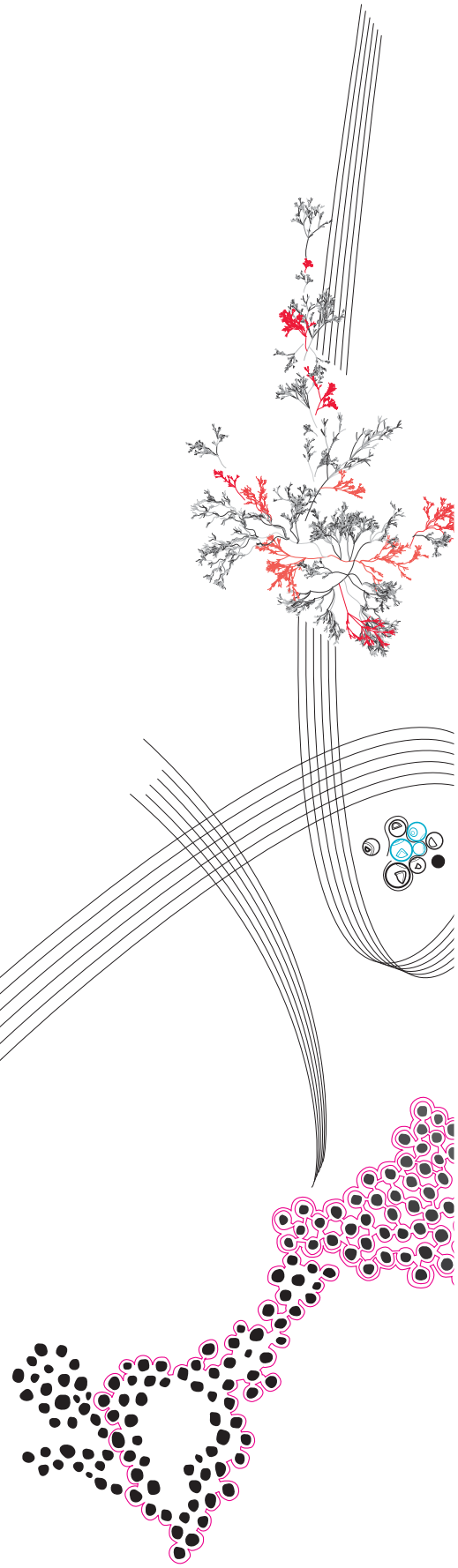

BSc Thesis Applied Mathematics
and Applied Physics

Spinning Pizza

M.D.J. Sent

Supervisors:
prof.dr. J.H. Snoeijer,
prof.dr.ir. B.J. Geurts,
dr. V. Sanjay

February, 2025

Department of Applied Mathematics
Faculty of Electrical Engineering,
Mathematics and Computer Science

Department of Physics of Fluids
Faculty of Science and Technology

UNIVERSITY OF TWENTE.

Spinning Pizza

M.D.J. Sent*

February, 2025

Abstract

A spun pizza dough tossed in the air stretches out by the action of centrifugal forces. As such, the spinning pizza offers an interesting case of sheet dynamics for a material of complex rheology. Here we study this problem using numerical simulations, treating the spinning dough as an axisymmetrically stretched Oldroyd-B fluid with infinite relaxation time. The model simulations reveal transients and stationary states, which are compared to theoretical predictions of stationary slender elastic bodies. While a qualitative agreement is achieved, significant quantitative differences arise. It is found that the slenderness of the initial shape and even a small amount of surface tension significantly influence the amount by which the pizza can stretch.

Keywords: Oldroyd-B, viscoelasticity, slender dynamics, Kelvin–Voigt solid, sheet dynamics, numerical simulations

1 Introduction

The stretching of sheets is a subject of study with both a practical use and a heuristic interest, occurring not only in industrial settings but also in natural and across a range of time and length scales. Examples include a model for the deformation of tectonic sheets (England and McKenzie 1982)[1], or the flow of a viscous fluid over a stretching surface which has many applications to industrial problems (Prasad *et al.* 2010). In an article by Howell, Scheid and Stone (2010)[3] the authors investigated a viscous sheet being spun about its axis. Figure 1.1 shows a figure from this article where we can see the time-evolution of the height profile of a viscous sheet being stretched by rotation. The tangible real-world analogue of this problem would be a pizza dough tossed in the air with a spin to stretch it (see figure 1.2), whence the article's name: Newtonian pizza. Here the word 'Newtonian' refers to the fact that the viscous sheet is modelled as a Newtonian fluid. The authors' main finding was that the viscous sheet, when stretched by being rotated, stretches to infinity in finite time. The authors noted a critical value in the rotational frequency relative to a resistive frequency above which the sheet would retract and below which the sheet would stretch indefinitely.

This article sparked Physics of Fluids at University of Twente to look into a similar problem but this time, instead of a viscous sheet, it would be an elastic blob (Sanjay, Bertin, Oratis, Snoeijer 2024)[5]. Moreover, the geometry was assumed to be slender, meaning that the 'dough's' shape is approximately flat except for a tiny edge. Typical shapes, now stationary in time, are reported in figure 1.3 (A). Different colors correspond to different dimensionless spinning rates. Not dissimilar to the result of Howell *et al.* (2010), the authors found a

*Email: m.d.j.sent@student.utwente.nl

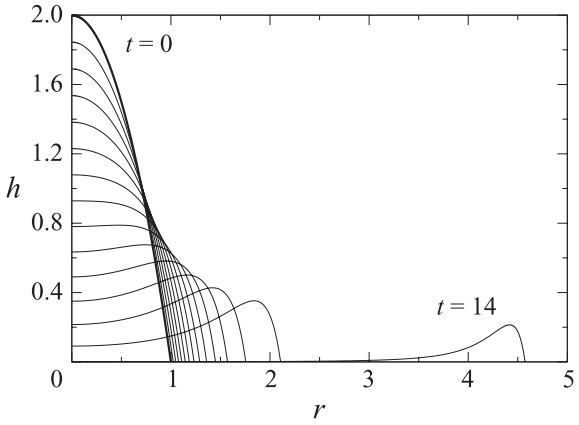

FIGURE 1.1: (Figure 2 from Howell *et al.* (2010): numerical result of the viscous sheet thickness profile h(r,t) versus the radial coordinate r. The initial shape is parabolic, $h_0 = 2(1-r^2)$.

FIGURE 1.2: A pizza dough being tossed in the air with a spin. Image courtesy of FreeImages[4].

nondimensional number with a critical value which determined whether the system has a stationary solution or if it instead diverges. This number, somewhat colloquially referred to as the Pizza number, will feature prominently in this report. It can be interpreted as a ratio of frequencies: the frequency to system is driven with, compared to a characteristic resistive frequency necessary for significant deformation. Whereas the resistive frequency in the case of Howell et al. (2010) stemmed from surface tension, Sanjay et al. (2024) found an elastic resistive frequency. Figure 1.3 (B) reports the maximum radius $r_{\max}$ for different spinning rates.

In reality, pizza dough or any bread dough for that matter, is not purely viscous nor purely elastic, but instead viscoelastic (Ng *et al.* 2006). Its elasticity stems from the long, cross-linked polymers of proteins and this is what makes dough retract to restore its shape after stretching. Its viscosity stems from the water which makes up the bulk of the dough's weight and this is what makes dough flow as a result of stress. There is no one kind of viscoelasticity, and the deformation of viscoelastic materials is an interesting and often non-trivial subject (see e.g. Doi 2013 [10]). As Sanjay *et al.* (2024) have investigated stationary states, it would be potentially interesting to see what happens to a viscoelastic material being spun about its axis over

time, from start to stationary state. The transient phase may involve interesting mechanics. This report utilises numerical solutions of a so-called Oldroyd-B model for viscoelastic fluids to attempt to answer the following questions:

- Are the simulations independent of the numerical discretisation parameters, such as the grid size and domain size?
- In what ways do the steady states of the simulation correspond to the stationary solutions of the slender model?
- Which parameters influence transient features and steady state features of the simulation, and in what way?

In section 2, we will pose the model used in the numerical experiments and briefly describe the simulation methodology. Section 3 covers the numerical verification of the model. In section 4, we will show and discuss the results of various numerical experiments. Section 5 closes the report with concluding remarks and an outlook on future possibilities.

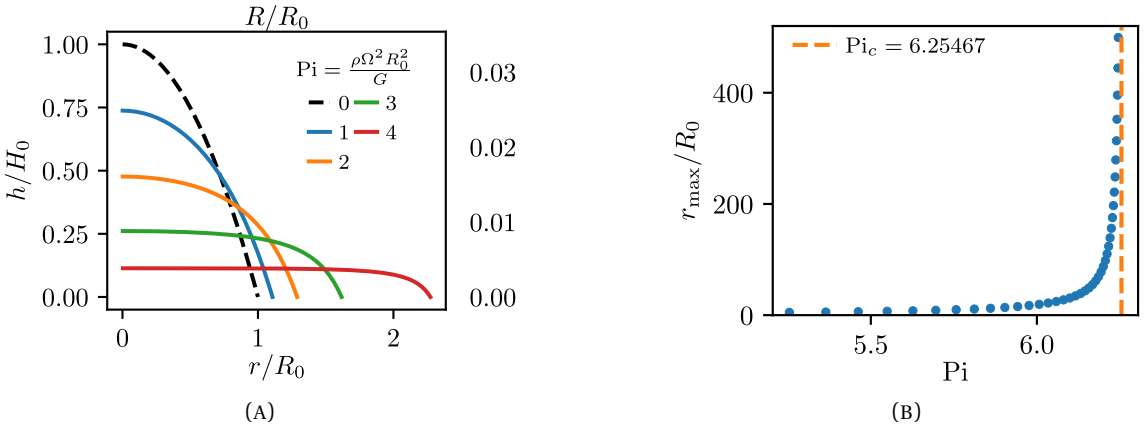

FIGURE 1.3: (A) Height profiles of the stationary solutions for different values of the Pizza number. The dashed line indicates the initial parabolic shape. Figure 1 from [5]. (B) At the critical Pizza number, or Pi, of approximately 6.25 the stationary solutions break down and the maximal radius of the blob starts to diverge. Figure 2 from [5]

2 Model

2.1 Control Parameters

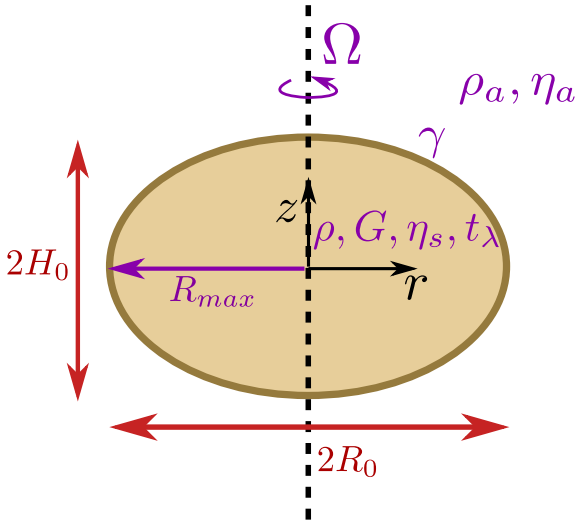

FIGURE 2.1: A schematic drawing of the viscoelastic material with surrounding air.

Figure 2.1 illustrates a schematic of the problem. The system consists of a blob of viscoelastic material, representing the pizza dough, and a surrounding Newtonian fluid which represents air. The blob is modelled as an Oldroyd-B viscoelastic fluid where ρ is the mass density, G the elastic shear modulus, η_s the material's background viscosity, t_λ the relaxation time and γ is surface tension. As for the air, ρ_a and η_a represent its mass density and dynamic viscosity, respectively. Ω is the rotational frequency which drives the blob's rotation. H_0 and R_0 are initial shape parameters, determining the initial height and width of the elliptical initial shape. $R_{\max}$ is the length one can draw from the axis of rotation to the maximally extended part of the blob. Throughout the report, we will keep track of $R_{\max}$ as a function of time.

To aid conceptual understanding and make simulations feasible we nondimensionalise the parameters as follows. R_0, G and ρ constitute the characteristic scales by which we scale other parameters. We obtain a characteristic frequency $\Omega_c = \sqrt{\frac{G}{\rho R_0^2}}$. This is the frequency required to significantly stretch the blob and it allows us define the "Pizza number"

$$\Pi = \left(\frac{\Omega}{\Omega_c}\right)^2 = \frac{\rho\Omega^2 R_0^2}{G}, \tag{1}$$

which may be understood as a ratio of frequencies, namely the driving rotational frequency over the resistive elastic frequency. The faster the rotation, the greater the Pizza number and the more our blob will be stretched. Moreover, we can obtain the elastocapillary number

$$Ec = \left(\frac{\Omega_\gamma}{\Omega_c}\right)^2 = \frac{\gamma}{GR_0} \tag{2}$$

which represents a balance of capillary to elastic stress. It, too, can be interpreted as a ratio of frequencies: the capillary frequency and the resistive elastic frequency. In the manner as defined above, a larger Ec corresponds to a more important contribution from surface tension relative to elastic stress. Throughout this report, Ec will be kept small, although we anticipate

that its influence will be non-negligible. The final two dimensionless parameters relate to relaxation and retardation times. They are the Deborah number

$$De = \frac{\Omega_c}{\Omega_\lambda} = t_\lambda \Omega_c = t_\lambda \sqrt{\frac{G}{\rho R_0^2}} \tag{3}$$

and the dimensionless retardation time

$$\tilde{t}_{\eta s} = \frac{\Omega_c}{\Omega_{\eta_s}} = t_{\eta s} \Omega_c = \left(\frac{\eta_s}{G}\right) \Omega_c = \frac{\eta_s}{\sqrt{\rho G R_0^2}}. \tag{4}$$

Retardation time expresses the delay of the system's elastic response to stress. For a perfectly elastic material, this elastic response is immediate and the retardation time is zero. An infinite retardation time corresponds to a liquid, which will never show an elastic response to stress. The Deborah number can be interpreted as nondimensional relaxation time, which is the counterpart to retardation time. The Deborah number indicates the delay of the system in showing a viscous response. A purely elastic material will never show a viscous response and therefore has infinite relaxation time. Throughout this report, the Deborah number will be kept very high compared to the timescale of our simulations. In fact, we will let it approach infinity. In this limit, the Oldroyd-B viscoelastic fluid becomes a Kelvin–Voigt solid.

Figure 2.2 shows the mechanical model with a parallel spring and dashpot used to represent the stress-strain response of a Kelvin–Voigt solid. The stress-strain response of a spring is $\sigma = G\varepsilon$ and that of a single dashpot is $\sigma = \eta\dot{\varepsilon}$. Because the spring and dashpot are placed in parallel, the total stress in the system as a response to strain is the stress in the spring added to the stress in the dashpot. The total stress-strain response of the system is thus $\sigma = \eta\dot{\varepsilon} + G\varepsilon$. In the limiting case of a Kelvin–Voigt solid, the equilibrium strain as a result of constant stress is completely determined by the spring (elasticity), and the dashpot (viscosity) has only a transient effect.

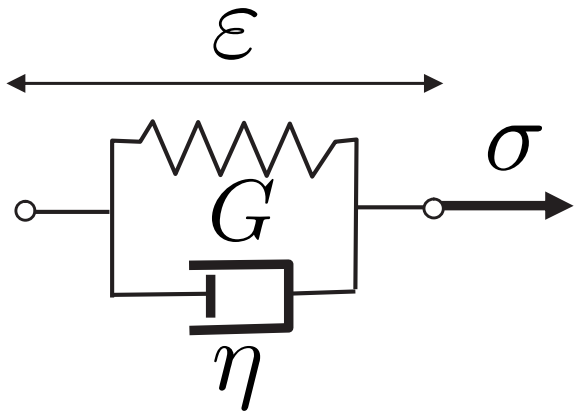

FIGURE 2.2: Mechanical model of a Kelvin–Voigt solid, consisting of a spring and a dashpot in parallel. σ is stress, ε is strain (extension) and G and η are the shear elastic modulus and viscosity, respectively. Image adapted from Doi (2013)[10].

2.2 Governing Equations

2.2.1 Mass and Momentum Conservation

An assumption we can make for soft deformable matter is that the flow is incompressible, meaning that mass density is constant always. Incompressible flow dynamics allow us to simplify the Navier–Stokes equations to

$$\text{mass conservation} \qquad \nabla \cdot \boldsymbol{u} = 0 \tag{5}$$

$$\text{momentum conservation} \qquad \rho\left(\frac{\partial \boldsymbol{u}}{\partial t} + \nabla \cdot (\boldsymbol{u}\boldsymbol{u})\right) = -\nabla p + \nabla \cdot \boldsymbol{\sigma} + f_b \tag{6}$$

where p is pressure and f_b represents a driving body force, which in our case is centrifugal force. $\boldsymbol{u}$ is the velocity vector and $\boldsymbol{\sigma}$ is the stress tensor, which depends on the constitutive equation, or the material's stress response to deformation, we use, which is described in subsection 2.2.2.

The air's mass density and dynamic viscosity should be far smaller than that of the blob and they are, throughout this entire report, expressed as a fraction of the blob's density and viscosity: $\frac{\eta_a}{\eta_s} = 0.01$ and $\frac{\rho_a}{\rho} = 0.001$. The domain's edges have an outflow boundary condition: as the blob is rotated and stretched, the air surrounding it can flow out of the box defined by the domain size.

2.2.2 Constitutive Relation

The simulation we work with makes use of the Oldroyd-B model for viscoelastic deformation. In this model, the stress tensor is divided into a stress from the elastic part, which stores energy, and one from the Newtonian solvent part, which dissipates energy,

$$\frac{\boldsymbol{\sigma}}{G} = (\boldsymbol{A} - \boldsymbol{I}) + \tilde{t}_{\eta s}\left(\tilde{\nabla}\tilde{\boldsymbol{u}} + (\tilde{\nabla}\tilde{\boldsymbol{u}})^T\right) \tag{7}$$

where $\boldsymbol{A}$ and $\boldsymbol{I}$ are the conformation tensor and the identity operator, respectively [7], and tildes denote dimensionless form. The conformation tensor is subject to the relaxation equation

$$\overset{\tilde{\nabla}}{\boldsymbol{A}} = -\frac{1}{De}(\boldsymbol{A} - \boldsymbol{I}) \tag{8}$$

where $\overset{\nabla}{(\cdot)}$ denotes the upper convected derivative[7]

$$\overset{\nabla}{\boldsymbol{A}} = \frac{d\boldsymbol{A}}{dt} + (\boldsymbol{u}\cdot\nabla)\boldsymbol{A} - \nabla\boldsymbol{u}\cdot\boldsymbol{A} - \boldsymbol{A}\cdot(\nabla\boldsymbol{u}). \tag{9}$$

The Oldroyd-B constitutive equation can be derived from a mesoscopic model of a dilute suspension of dumbbells in a Newtonian solvent.[11] Polymers are modelled as two beads connected by a Hookean spring, which resembles a dumbbell. As the surrounding solvent flows, the beads are dragged along and the restoring force of the spring describes the way that a viscoelastic substance has an elastic component, which tries to restore deformation.

2.3 Basilisk

For the simulations, we make use of the free software programme Basilisk C[8]. Basilisk C uses adaptive mesh refinement (AMR) where we can refine the grid based on estimated errors

in interface location, curvature, velocity field, and elastic stresses. The maximum level of refinement “Maxlevel" controls the size of the finest grid employed using $\Delta_{\min} = L_0/2^{\text{Maxlevel}}$ where L_0 is the length of the domain. We can interpret $N = \text{int}(1/\Delta)$ as the number of grid cells per unit length that would be required to get the same accuracy on a uniform grid. The domain size L_0 is expressed in terms of the characteristic length scale R_0. A domain size of R_0 means that one quadrant is R_0 long and tall, and the total domain has dimensions $2R_0$ by $2R_0$. For the details of the numerical aspects of the code, we refer the reader to the GitHub repository for this project.[9]

2.4 Example

To aid in visual understanding, this subsection shows the time sequence of a typical simulation, with the parameters used listed in table 1.

Π	4
Domain size	$4R_0$
$\tilde{t}_{\eta s}$	0.5
De	10^{30}
N	2^8
H_0/R_0	0.5

TABLE 1: The parameters used for the results in subsection 4.3

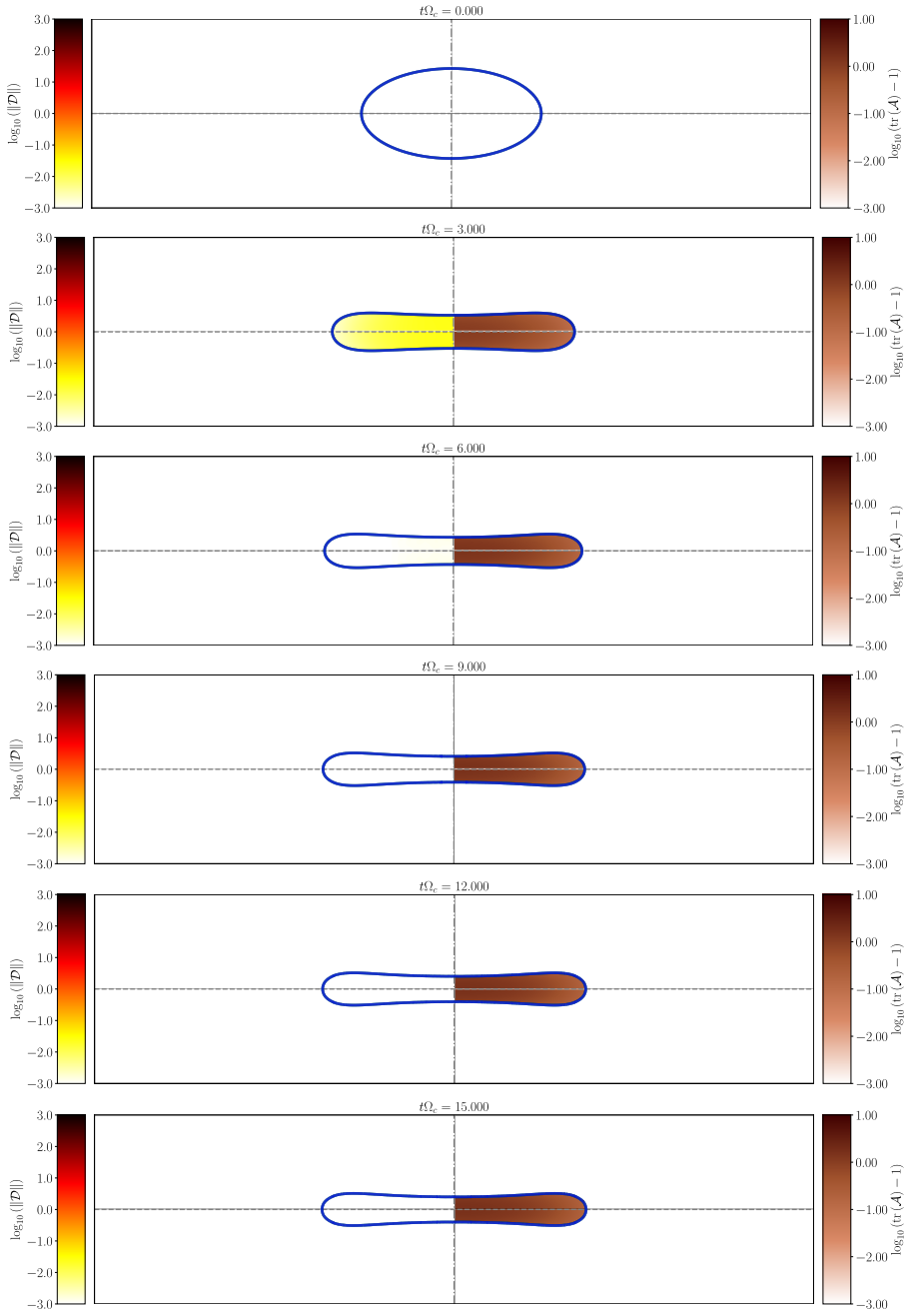

FIGURE 2.3: Snapshots of a typical simulation. The right hand side shows a measure of stored energy and the left hand side shows a measure of dissipated energy.

3 Numerical Verification

3.1 Spatial Grid Refinement

As a first step, to test the accuracy and convergence of our numerical simulations, we vary the number of spatial grid cells in our domain to see the effect on the outcome of a simulation. For the following experiment, we use the parameters as listed in table 2. They are chosen so that there is a steady state that is noticeably deformed from the initial condition but the Pizza number is not yet in the range where we would start to expect a breakdown of steady states.

This is based on the slender theory which predicts the critical Pizza number being approximately 6.25 as in figure 1.3 (B). Beyond this critical value there are no steady states.

Π	4
Domain size	$4R_0$
$\tilde{t}_{\eta s}$	0.5
De	∞
Ec	0.01
H_0/R_0	1

TABLE 2: The parameters used in subsection 3.1

The domain is not divided in a uniform grid, but rather an adaptive grid which increases resolution near the interface between the Kelvin-Voigt solid and the Newtonian fluid. The snapshots shown in figures 3.3 and 3.4 allow us to see by inspection that the general behaviour of the simulation does not change much as a result of a finer resolution, although the interface in figure 3.4 is much better resolved and expected to the corresponding analytical solution. To get into greater detail regarding the numerical convergence upon grid refinement, let us look at $R_{\max}$, kinetic energy and $\frac{d}{dt}R_{\max}$ as functions of time for a range of spatial resolutions.

Figures 3.1 (B) and 3.2 show that qualitatively we are indeed near a steady state, with kinetic energies at a level where we would no longer expect any significant deformation and a rate of change of $R_{\max}$ that has approached 0. Here one can observe a small qualitative difference for different resolutions. The rate of change of $R_{\max}$ has dropped slightly below 0 for the lower resolutions, most clearly so for N = 2^5. This implies a slight contraction reminiscent of an underdamped system, whereas the simulations with finer resolutions appear to converge to a critically damped system. For a quantitative comparison we turn to figure 3.1 (A) where we see the evolution over time of $R_{\max}$. The difference between the resolution N = 2^8 and a lower resolution is defined as

$$\frac{1}{t_{\max}}\sqrt{\sum_{i=0}^{2000}\left(R_{\max}(i,N=2^8)-R_{\max}(i,N)\right)^2 t_{\text{snap}}} \tag{10}$$

where $t_{\max}$ = 20 denotes the total time interval and t_{snap} = 0.01 denotes the sampling time interval. The inset in figure 3.1 (A) reveals an ever-smaller difference for every increase in resolution. From N = 2^6 to N = 2^7, the difference with N = 2^8 is roughly halved, although the decrease in error we observe going from N = 2^5 to N = 2^6 is closer to a quarter. This suggests that we work with a first order method, which reaches its asymptotic convergence rate for N beyond 2^5.

The simulation for N = 2^8 behaves as expected and smoothly for not too great computation time. Typical computation times for this resolution are in the range of 3-4 days, whereas for N = 2^9 the computation times grow into the range of 10-12 days for little gain in accuracy. This is not feasible to work with, and for our purposes not required. Therefore, going forwards in the experiments in this report, we shall use a resolution of N = 2^8.

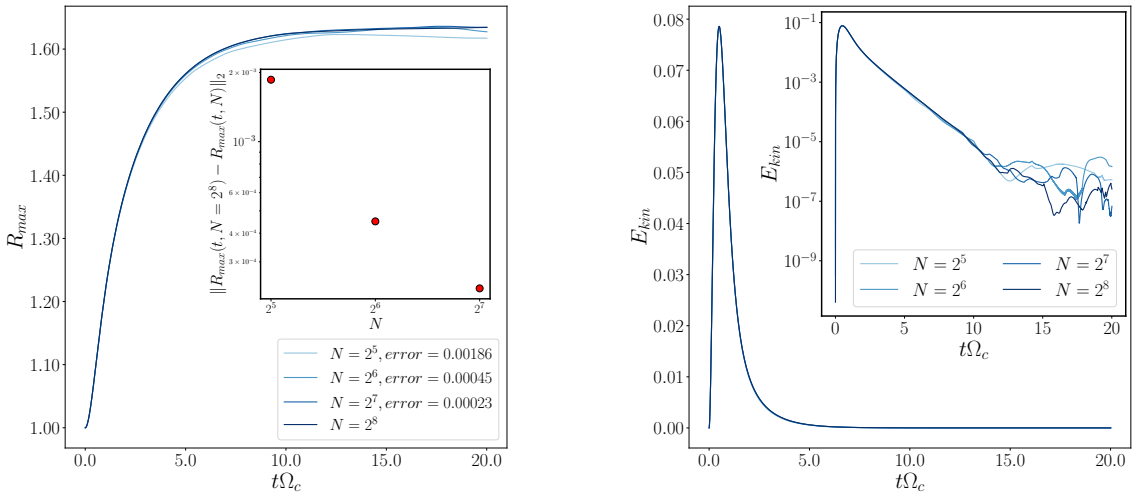

(A) (B)

FIGURE 3.1: Maximal radius with log-scale inset (A) and kinetic energy with semilog-scale inset (B) over time for different numbers of grid cells per unit length N. The error in $R_{\max}$ is defined as in equation 10. The kinetic energy at the end of the simulation close to zero, which is too low to cause significant changes in the relevant time-scale.

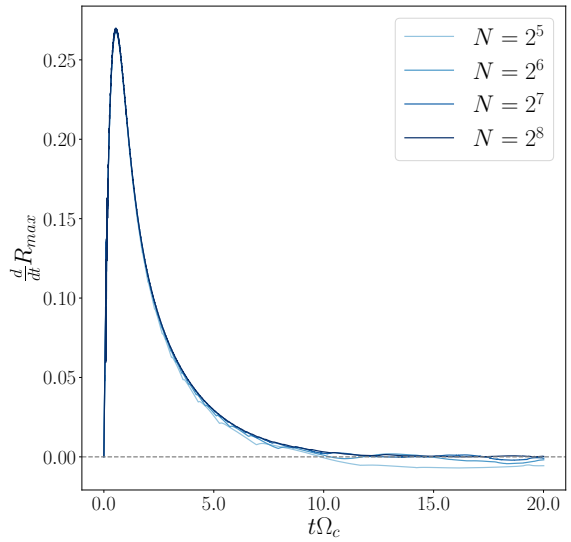

FIGURE 3.2: Growth rate of maximal radius over time for different numbers of grid cells per unit length N. The dashed line indicates a growth rate of 0.

3.2 Varying Domain Size

In this subsection we will vary the domain size of our simulation to see whether or not imposing a finite domain affects the outcome. If everything is properly dimensioned, then the outcome should not depend on domain size so long as the blob remains separated well enough from the domain boundary. In our case, domain size is defined as the size of one quadrant's width and height in terms of the initial radius R_0. The domain size Ldomain = 4 means that one quadrant is $4R_0$ long and tall, and the total domain has dimensions $8R_0$ by $8R_0$. We use the same parameters as in subsection 3.1, listed in table 3. The number of spatial grid cells is adjusted to keep the number per unit length the same for all domain sizes.

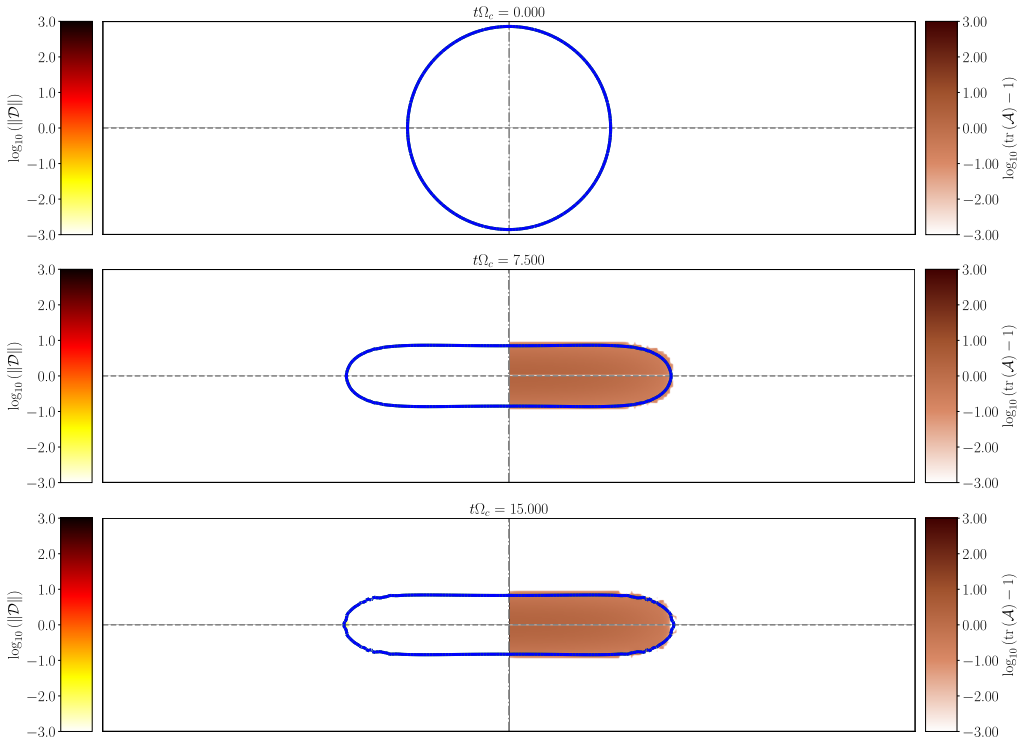

FIGURE 3.3: Snapshots of a simulation with N = 2^5 grid cells per unit length (R_0).

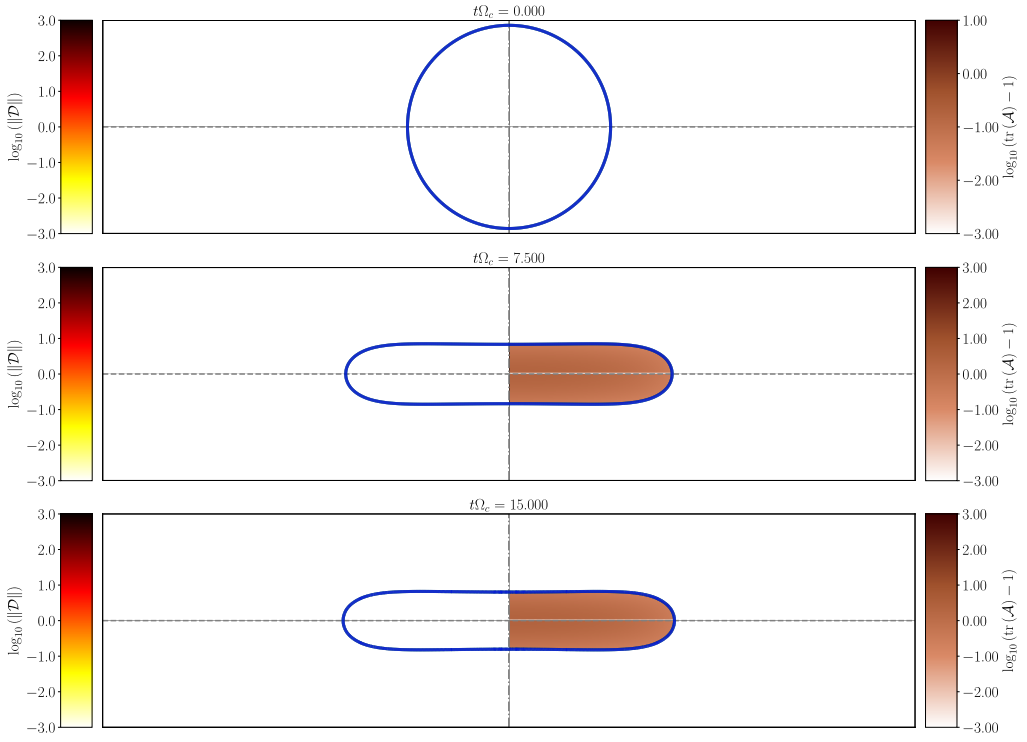

FIGURE 3.4: Snapshots of a simulation with N = 2^8 grid cells per unit length (R_0).

Figures 3.5 and 3.6 show a very clear overlap for $R_{\max}$, kinetic energy and the rate of change

Π	4
$\tilde{t}_{\eta s}$	0.5
De	∞
Ec	0.01
H_0/R_0	1
N	2^8

TABLE 3: The parameters used in subsection 3.2

of $R_{\max}$ over time. This result reassures us that the simulation's outcome does not noticeably depend on an increased domain size. Given that we are using boundary outflow and the surrounding medium is air, it is not surprising that the domain size has a negligible influence on the dynamics of the blob.

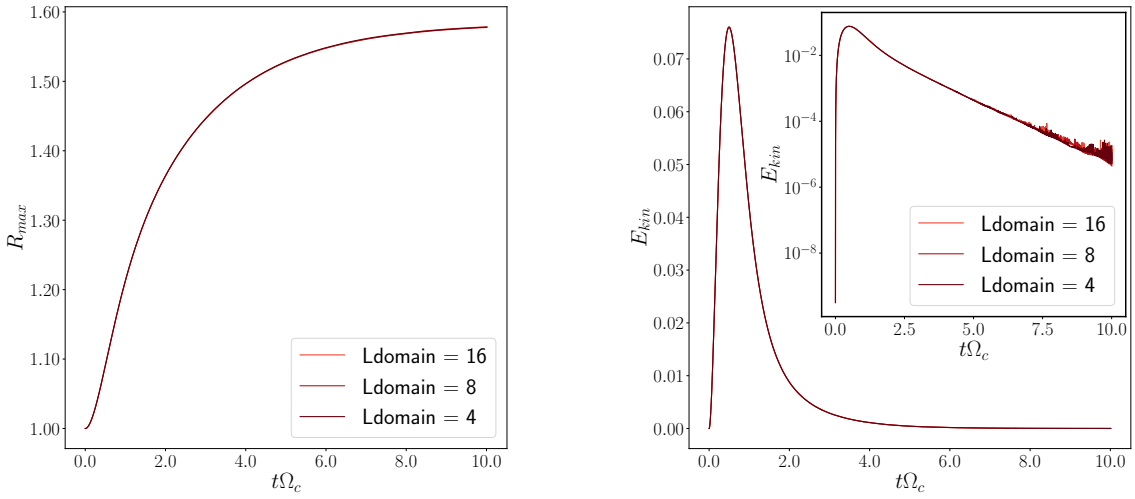

(A) (B)

FIGURE 3.5: Maximal radius with log-scale inset (A) and kinetic energy with semilog-scale inset (B) over time for varying domain sizes.

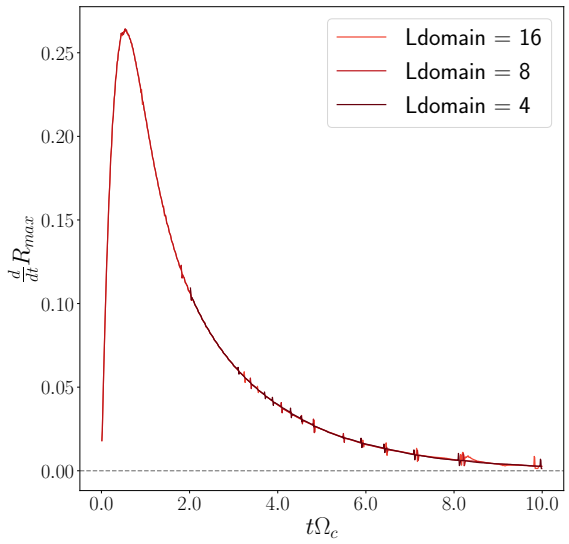

FIGURE 3.6: Growth rate of maximal radius over time for varying domain sizes. The bumps are an artefact from an older post-processing method to obtain the growth rate. A updated method was used in figure 3.2, where the bumps are less pronounced.

4 Results

4.1 Varying Dimensionless Retardation Time $\tilde{t}_{\eta s}$

Viscous effects in a Kelvin–Voigt solid's response to stress are transient, and are expected to give a dampening effect with an exponential decay. Viscosity may cause over- or underdamping, but so long as there is viscosity to dissipate energy in the model, a Kelvin–Voigt solid will tend to some steady state deformation as a response to constant stress, and the magnitude of deformation will be determined by the elastic shear modulus. To study the transient effects of our model, therefore, we adjust the dimensionless retardation time $\tilde{t}_{\eta s} = (\frac{\eta_s}{G})\Omega_c$. The elastic shear modulus G is one the characteristic scales, so a variation in $\tilde{t}_{\eta s}$ is akin to a variation in viscosity η_s.

Figure 4.1 shows the dissipation of kinetic energy for three different values of $\tilde{t}_{\eta s}$. Other parameters used are listed in table 4. There is exponential decay of the kinetic energy, meaning that the system indeed approaches a steady state. The higher the dimensionless retardation time, the slower the decay. We remind the reader that retardation time expresses the delay of a system's elastic response to stress. With this in mind, a higher retardation time corresponding to a slower decay agrees with our understanding of the system because it takes longer for the viscous effects to have passed. The steady state corresponds to the system's elastic response and its onset is delayed for greater retardation time.

Throughout the following experiments, we will use $\tilde{t}_{\eta s} = (\frac{\eta_s}{G})\Omega_c = 0.5$. For the motivation of using this value, we refer the reader to the Appendix.

4.2 Slenderness and $R_{\mathbf{max}}$

We now turn to simulation for which the initial aspect ratio $\frac{H_0}{R_0}$ is varied from 1, which corresponds to a perfectly circular shape, to more and more slender ellipses ($H_0/R_0 < 1$). The slender theory prediction (Sanjay *et al.* 2024[5]) relies on the assumption that the initial shape of

Π	4
Domain size	$4R_0$
De	∞
Ec	0.01
N	2^8

TABLE 4: The parameters used for the results in subsection 4.1

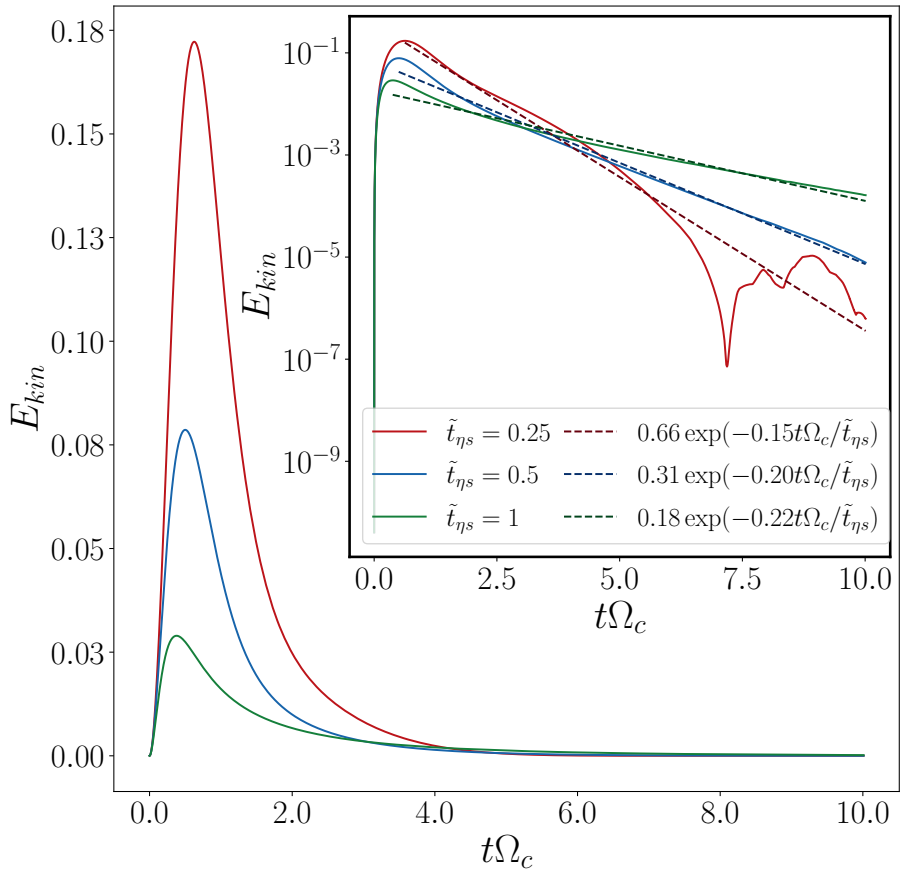

FIGURE 4.1: Kinetic energy for several values of the Ohnesorge number and corresponding fits of the exponential decay of the form $A\exp(-kt)$, with A a prefactor of the magnitude and $-k$ the decay rate.

the blob is slender, meaning thin and flat except for a small edge. From the numerical verification experiments we already have seen that the steady state $R_{\max}$ tends to approximately 1.63 for $\Pi = 4$ (see figure 3.1 (A)). This is, in fact, significantly lower than what is predicted from the slender theory: a steady state $R_{\max}$ of approximately 2.27 for $\Pi = 4$ as can be seen in figure 1.3 (A) [5]. One could argue, therefore, that it might be that it is the decidedly non-slender, circular initial shape which may affect the steady state outcome. If we adjust the initial shape to be more slender, should we not expect our outcome to get closer to the theoretical prediction?

As it turns out, as may be seen from figure 4.2, the opposite is the case. Panel A shows the time evolution of $R_{\max}$ for different aspect ratios and panel B reports $R_{\max}(t\Omega_c = 15)$ as a function of the inverse aspect ratio. The lower the aspect ratio, the lower the steady state $R_{\max}$. If we compare our model to the slender theory prediction[5], we recognise a distinct difference

in the assumptions, namely that of capillarity. For the slender theory, surface tension is not taken into account, but its presence makes it so that there is a restoring force which minimises the interface area. Figure 4.3 shows the initial and final shapes for the various aspect ratios. The more slender our blob, the further away it is from being circular, i.e. having minimal surface area. The effect of this is that the more slender our blob is, the more important surface tension becomes. Like elastic stress, it acts as a restoring force, working against the growth of $R_{\max}$. Subsection 4.3 therefore explores the effect of adjusting the elastocapillary number, to explore the influence of surface tension.

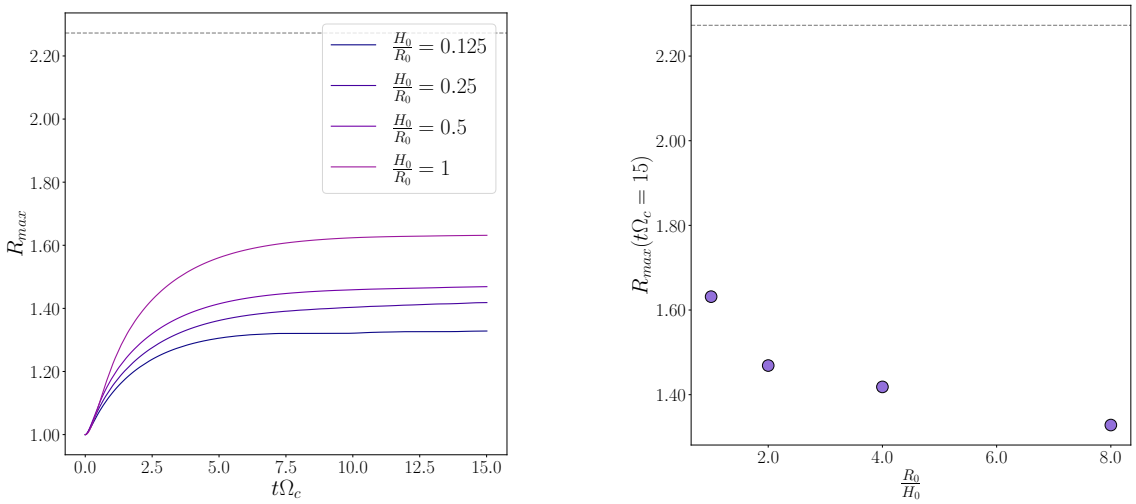

(A) (B)

FIGURE 4.2: (A) $R_{\max}$ over time for several aspect ratios ranging from a circular initial shape to more slender elliptical initial shapes. The dashed grey line indicates the prediction from the slender theory of $R_{\max}$ in the steady state. (B) $R_{\max}$ at $t\Omega_c = 15$ plotted against the inverse of the aspect ratio. Again, the dashed grey line indicates the slender theory prediction.

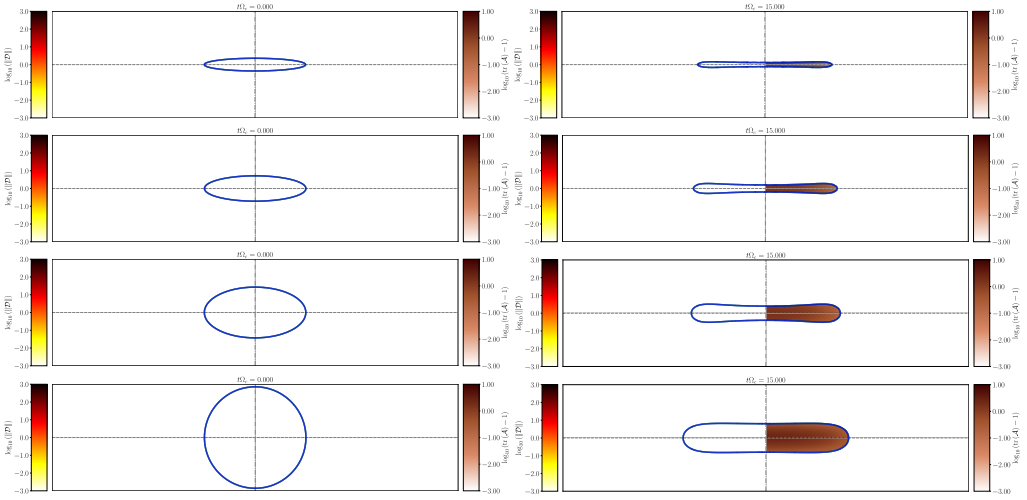

FIGURE 4.3: Snapshots of the initial state to the state at $t\Omega_c = 15$ for an aspect ratio of (from top to bottom) 0.125, 0.25, 0.5, 1.

Π	4
Domain size	$4R_0$
$\tilde{t}_{\eta s}$	0.5
De	∞
Ec	0.01
N	2^8

TABLE 5: The parameters used for the results in subsection 4.2

4.3 Slenderness and Ec

In this section we turn to simulations of four cases, consisting of different aspect ratios and two different values of the elastocapillary number Ec. Figure 4.4 shows the evolution of $R_{\max}$ over time for these four cases again compared with the slender theory prediction from Sanjay *et al.* (2024) [5]. The blue graph corresponds to the circular initial shape and an Ec of 0.01, the value used in all previous simulations thus far. For the same aspect ratio but a lower Ec, we turn to the red graph which shows that $R_{\max}$ approaches a higher steady state value, although the effect is not very pronounced and $R_{\max}$ does not come much closer to the slender theory prediction. The orange graph shows $R_{\max}$ over time for the slender initial shape and an Ec of 0.01.

For the same aspect ratio but a lower Ec, we turn to the green line, which reports a dramatic change in the time-evolution of $R_{\max}$. First it shows a similar behaviour to the other graphs, but instead of flattening it grows on steadily until its growth rate increases somewhat. Finally, around $t\Omega_c = 30$ it appears to have reached an equilibrium relatively near the slender theory prediction. Interestingly, $R_{\max}$ proceeds to shoot up at a faster rate than it has done before. The origin of this behaviour is revealed in the snapshots in figure 4.5. There we see that a small droplet has broken off from the blob and has started flying off a result of the centrifugal force from the imposed angular frequency. The droplet may have been pinched off as a result of surface tension, although the atomisation may also be a result of insufficient resolution in the spatial grid. The blob itself has reached an equilibrium and is stretched no further. The steep increase in the green graph in figure 4.4 can be explained as a post-processing mistake: in tracking $R_{\max}$ we have not taken the break-off of a tiny droplet due to a numerical artefact into account, so the position of the nucleated droplet is reported as $R_{\max}$. This result has come in very shortly before the end of this assignment, so we would also instill in the reader a sense of caution when it comes to the numerical validity of this result.

The uncertainty around the atomisation notwithstanding, we can carefully say that the elastocapillary number is of influence on the steady state $R_{\max}$, and its effect is magnified by slender initial conditions. Whether or not the slender prediction is approached in the limit of vanishing surface tension remains to be investigated.

Π	4
Domain size	$4R_0$
$\tilde{t}_{\eta s}$	0.5
De	∞
N	2^8

TABLE 6: The parameters used for the results in subsection 4.3

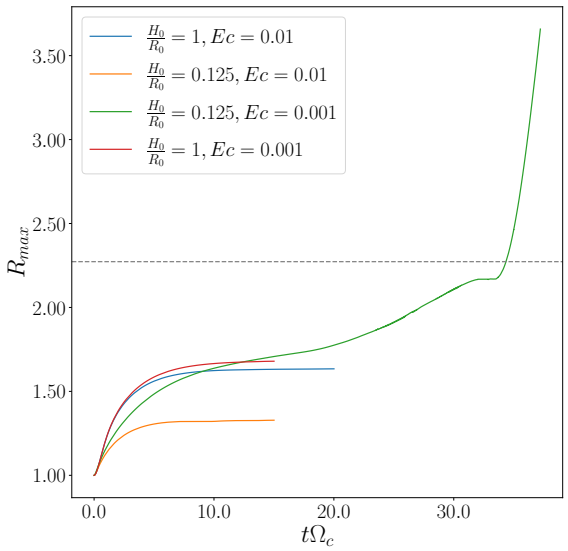

FIGURE 4.4: $R_{\max}$ over time for four combinations of aspect ratio and Ec. The grey dashed line indicates the slender theory prediction of approximately $R_{\max} = 2.27$[5].

5 Conclusion and Outlook

The aim of this project was to explore numerical simulations of a spinning blob of Oldroyd-B fluid with infinite relaxation time, to model a tossed pizza dough, and to compare the simulation results to theoretical predictions of the stationary states based on the assumption of slender dynamics and neglected surface tension.

The numerical solutions of our rotated blob were found to be independent of the discretisation parameters grid resolution and domain size (as discussed in section 3). The simulations also showed that the maximal radius, after a transient growing phase, approaches an equilibrium state determined by a balance of inertial forces and elasticity. Nevertheless, we found a difference in the simulations' steady state solution compared to the stationary solutions from the slender theory prediction in Sanjay *et al.* (2024)[5]; namely, that the maximal radius did not extend as far in our simulations as predicted theoretically. In fact, at the start of this project, our aim was to perform numerical experiments that explore the breakdown of stationary states as we approach the critical condition of the Pizza number, as can be seen in figure 1.3 (B). The simulations' steady states not corresponding to those theoretically predicted spurred us to investigate whether specific parameters were the cause of this difference, as well as to investigate the transient phase.

This transient phase was explored in subsection 4.1. The retardation time of a system affects the transient phase of the system, where the rate of exponential decay of the system's kinetic energy agrees with the exponential decay in a Kelvin–Voigt solid. Curiously, the retardation time appears not only to influence the transient phase, but also the steady state (see the Appendix). In section 4.2 and 4.3 we explored the effect of slenderness of the initial shape on the growth of $R_{\max}$. A more slender initial shape was found to result in a steady state maximal radius that is further from, not closer to, the prediction from the slender theory. Interestingly, as reported in figure 4.4, a slender initial shape combined with a lower elastocapillary number was found to result in an $R_{\max}$ much closer to the slender theory prediction. This result, however, was found only very late in this project's timeline. We could not, therefore, test the

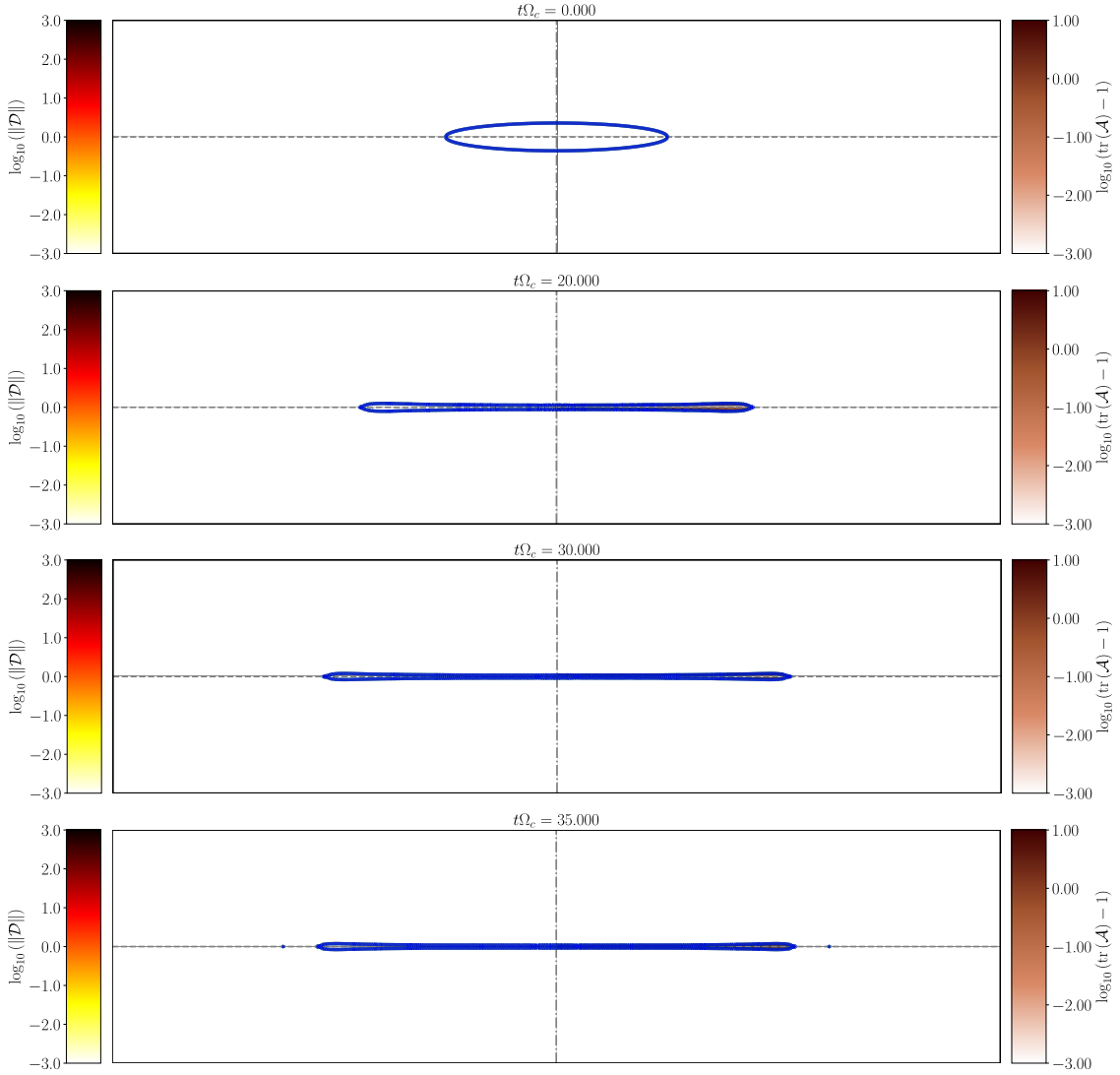

FIGURE 4.5: Several snapshots of the simulated case with aspect ratio $\frac{H_0}{R_0} = 0.125$ and $Ec = 0.001$, corresponding to the green graph in figure 4.4. At $t\Omega_c = 30$ an equilibrium has been reached, but the edge has obtained a pointy shape, with a protrusion starting to form. At $t\Omega_c = 35$ the protrusion has come loose from the rest of the blob and has begun to fly off as a result of centrifugal force.

cause of this behaviour more thoroughly within the time permitted.

As an outlook for future research, then, a good place to start would be an investigation into the case of low Ec and a slender initial shape. Are the outcomes of this case still independent of discretisation parameters, or is the pinching off of the tip a result of insufficient resolution? Does the system respond differently for a variation in retardation time than for the non-slender, higher Ec case as shown in subsection 4.1? Another parameter worth looking into is the Pizza number. There was not enough time in this project to sweep over the Pizza number and note the resulting outcome of the steady state $R_{\max}$ as we approach and exceed the critical Pizza number from the slender theory prediction (figure 1.3 (B)). Will we see a breakdown of steady states at the critical Pizza number, or will the steady states start to break down for a lower Pizza number already? We wish to note that there are practical difficulties involved in

determining whether there exists a steady state or not as we increase the Pizza number. As $R_{\max}$ grows close to the domain boundary, the simulation ends and we must try again with a larger domain size, and adjust the number of grid cells accordingly to keep N, the number of grid cells per unit length, equal. The larger the domain size, the longer the computation time, therefore. It is possible that one needs many iterations of adjusting the domain size until one can verify that $R_{\max}$ indeed approaches a steady state, which could take a lot of computation time.

As a final outlook for future research, we turn to the slender theory. As shown in subsection 4.3, a variation in elastocapillary number combined with slender initial conditions can influence the growth of $R_{\max}$ significantly. It could be interesting to adjust the governing equations in the slender theory model to include capillarity and investigate how that affects the stretching of the blob in the steady state.

6 Appendix

This section reports the effects of varying retardation time on the time-evolution of $R_{\max}$. The parameters used in this section are listed in table 7. Figure 6.1 (A) shows the time-evolution of $R_{\max}$ for the different retardation times, corresponding to different viscosities in the system when viewed as a Kelvin–Voigt solid (see figure 2.2). We see that for very low viscosity (low $\tilde{t}_{\eta s}$), the system is underdamped and oscillates before converging on a steady state. Figure 6.1 shows the kinetic energy over time, with an exponential decay as discussed in subsection 4.1, and the oscillations are clearly visible as bounces in the semilog-scale inset.

What was not expected, was the dependence of the steady state $R_{\max}$ on the retardation time. If we view the system as a Kelvin–Voigt solid, retardation time represents the delay of the system's elastic response: after enough time has passed, only the system's elasticity determines how far the system stretches as a result of constant stress. Particularly the cases of $\tilde{t}_{\eta s} = 0.1$ and $\tilde{t}_{\eta s} = 0.01$ in figure 6.1(A) are curious. As we go down in $\tilde{t}_{\eta s}$, the steady state $R_{\max}$ appears to increase, but for these two values the system oscillates around a lower $R_{\max}$. We do not know why our system exhibits this behaviour. For the results in subsections 4.2 and 4.3, we compare $R_{\max}$ for different cases. We have therefore decided not to use lower values of $\tilde{t}_{\eta s}$ for these experiments because we wish to stay away from effects we do not understand. Instead, we have decided to use $\tilde{t}_{\eta s} = 0.5$

Π	4
Domain size	$4R_0$
De	∞
N	2^8
Ec	0.01

TABLE 7: The parameters used for the results in the Appendix.

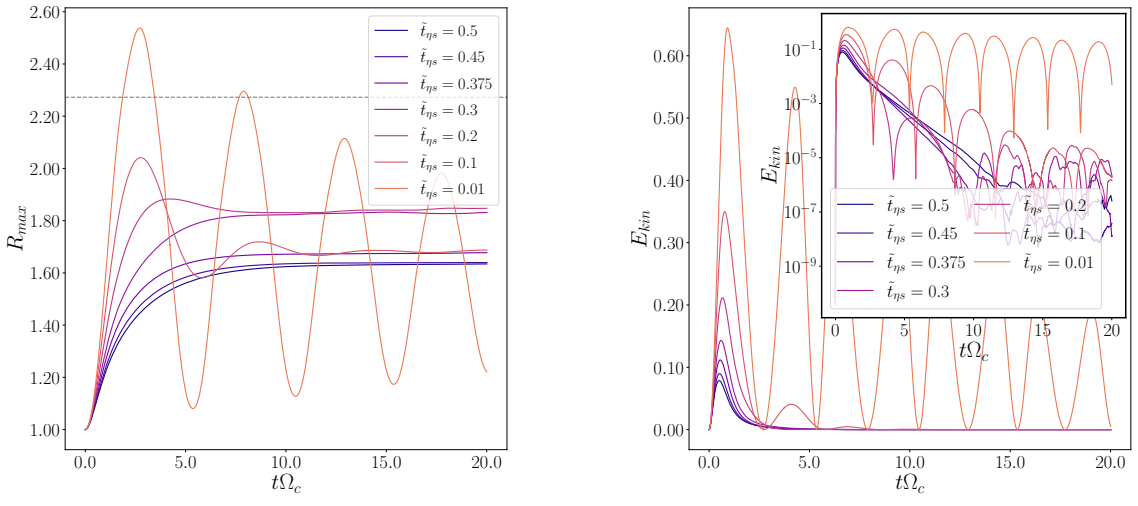

(A) (B)

FIGURE 6.1: Maximal radius (A) and kinetic energy with semilog-scale inset (B) over time for different values of the dimensionless retardation time $\tilde{t}_{\eta s} = \frac{\eta_s}{G}\Omega_c$.

References

[1] England P., McKenzie D., *A thin viscous sheet model for continental deformation*, Geophysical Journal International, vol. 70, no. 2, pp. 295–321, doi: 10.1111/j.1365-246X.1982.tb04969.x. (1982)

[2] Prasad K. V., Vajravelu K., Datti P. S., *Mixed convection heat transfer over a non-linear stretching surface with variable fluid properties*, International Journal of Non-Linear Mechanics, vol. 45, no. 3, pp. 320–330, doi: 10.1016/j.ijnonlinmec.2009.12.003. (2010)

[3] Howell, P. D., Scheid, B., Stone, H. A., *Newtonian pizza: spinning a viscous sheet* Journal of Fluid Mechanics, vol. 659, pp. 1-23, https://doi.org/10.1017/S0022112010001564 (2010)

[4] wmstadler (username), *Tossing pizza dough at Straight From New York pizza in Salem, Oregon, USA* [Photograph], FreeImages, https://www.freeimages.com/photo/tossing-pizza-dough-1-1057356, accessed 29-01-2025

[5] Sanjay, V., Bertin. V., Oratis, A. T., Snoeijer, J. H., *Spinning Elastic Pizza*, private communication (2024)

[6] Ng, T. S. K., McKinley, G. H. ,Padmanabhan, M., *Linear to Non-linear Rheology of Wheat Flour Dough*, Applied Rheology, vol. 16, no. 5, pp. 265–274, doi: 10.1515/arh-2006-0019. (2006)

[7] Macosko, C. W., *Rheology - Principles, Measurements and Applications - 4. Nonlinear Viscoelasticity* John Wiley & Sons. (1994)

[8] Popinet S. and collaborators, *Basilisk C*. https://www.basilisk.fr (Last accessed: 12-11-2024), 2013-2025

[9] Sanjay V., *Code Repository: Viscoelastic Pizza*, https://github.com/comphy-lab/Viscoelastic-pizza (Last accessed 2-12-2024) 2024-2025

[10] Doi, M., *Soft Matter Physics - 9. Flow and Deformation of Soft Matter*, Oxford University Press, https://doi.org/10.1093/acprof:oso/9780199652952.003.0009 (2013)

[11] Castillo Sánchez, H. A.; Jovanović, M. R.; Kumar, S.; Morozov, A.; Shankar, V.; Subramanian, G.; Wilson, H. J. *Understanding Viscoelastic Flow Instabilities: Oldroyd-B and Beyond*. Journal of Non-Newtonian Fluid Mechanics, 302, 104742. https://doi.org/10.1016/j.jnnfm.2022.104742. (2022)

Acknowledgements

I wish to thank my committee first of all. A double degree bachelor project involves two departments, five committee members of whom three are supervisors. In such situations, planning can be difficult and I am grateful for everyone's flexibility to make this project happen. I thank my supervisors for the fruitful discussions we have had, often bridging mathematics and physics. In particular I thank my daily supervisor Vatsal for his endless patience with me, a near hopeless case when it comes to programming and anything computer related. I have learnt more about programming and software in the first two weeks of this project, than I would otherwise have learnt in a couple of years.

I thank the Physics of Fluids group for accommodating me for the duration of my project. I have felt welcome from day one. I especially wish to thank Nienke and Coen, for the ever engaging chats we have had both during tea breaks and outside of them.

Of course I thank my friends, notably my study friends: Randy, for general mayhem, Niek, for the memorable drink "tasting" sessions, Niels, because it is wonderful to have someone with a similar appetite for political conversation, Mathijs, for being a close friend at a long distance, and Thomas, for his sprezzatura.

Lastly, I thank my family for always being there, especially my parents with whom I am always welcome.